nature photonics

ARTICLES

https://doi.org/10.1038/s41566-020-00704-8

Pockels soliton microcomb

Alexander W. Bruch[1], Xianwen Liu[1], Zheng Gong[1], Joshua B. Surya[1], Ming Li[2], Chang-Ling Zou[2] and Hong X. Tang[1]✉

Kerr soliton microcombs have recently emerged as a prominent topic in integrated photonics and have enabled new horizons for optical frequency metrology. Kerr soliton microcombs, as the name suggests, are based on high-order cubic optical nonlinearity. It is desirable to exploit quadratic photonic materials, namely Pockels materials, for soliton generation and on-chip implementation of 1*f*–2*f* comb self-referencing. Such quadratically driven solitons have been proposed theoretically, but have not yet been observed in a nanophotonic platform, despite recent progress in quadratic comb generation in free-space and crystalline resonators. Here, we report photonic-chip-based Pockels microcomb solitons driven by three-wave mixing in an aluminium nitride microring resonator. In contrast to typical Kerr solitons, the Pockels soliton features unity soliton generation fidelity, two-by-two evolution of multi-soliton states, favourable tuning dynamics and high pump-to-soliton conversion efficiency.

Within the past decade, Kerr microcombs based on $\chi^{(3)}$ optical nonlinearity have made a phenomenal transition from laboratory curiosity to a field of study in their own right[1]. Tight optical confinement and facile geometrical dispersion control afforded by nanophotonic waveguides have achieved significant milestones in nonlinear optics and comb development in a chip-scale package[2]. Today, these 'gold standard' Kerr combs are reaching into application spaces such as optical frequency synthesis[3], optical clocks[4,5], exoplanet observation[6,7], chemical spectroscopy[8,9] and quantum optics[10]. Many of these applications leverage the low-noise Kerr soliton state, where the comb lines become mutually phase-locked and form an optical pulse in the time domain[11–13]. The exploitation of the lowest order $\chi^{(2)}$ optical nonlinearity, on the other hand, can bring about additional novel phenomena in frequency comb development. Frequency doubling of a Kerr comb allows for efficient near-visible[14,15] and ultraviolet[16] comb generation as well as direct detection of a comb's carrier envelope offset frequency[17]. Nonlinear coupling between the fundamental and second-harmonic bands[14,18] also introduces a dissipative energy transfer pathway to new wavelengths, similar to that seen in the case of Raman–Stokes solitons[19].

Frequency comb-like spectra arising solely from $\chi^{(2)}$ nonlinearity have been predicted theoretically for nearly two decades in a degenerate optical parametric oscillator[20]. Such quadratic combs were only recently demonstrated in bulk optical cavities containing only $\chi^{(2)}$ nonlinearity[21–24] operating in a second-harmonic generation (SHG) scheme. These combs arise from back-to-back second-harmonic/sum-frequency generation (SHG/SFG) and optical parametric oscillation (OPO). The process may also proceed in the reverse case (OPO followed by SHG/SFG) as in refs. [21,24]. Cascaded three-wave mixing between frequency components yields comb lines separated by the cavity free spectral range (FSR), as in the case of the Kerr frequency comb. These so-called 'quadratic frequency combs' enjoy a relatively low power threshold and high pump-to-comb efficiency due to the inherently large magnitude of the $\chi^{(2)}$ susceptibility compared to the $\chi^{(3)}$ one. Additionally, the cascaded SHG/SFG-OPO process creates a frequency comb at both the fundamental and harmonic frequencies, naturally giving rise to dual-band comb spectra. These bulk cavities may also give rise to interesting temporal phenomena such as temporal simultons[25].

The potential benefits of quadratic frequency combs have ushered a flurry of numerical studies on the dynamics of combs driven by $\chi^{(2)}$ nonlinearity. Numerical simulations of quadratic combs have revealed modulation instability (MI) regimes and nonlinear bistability akin to a Kerr frequency comb[24,26], as well as low-noise Turing patterns including multiple soliton states[27]. Similar dynamics have recently been studied in a microresonator system operating in SHG-driven[28] and OPO-driven[29] schemes. In particular, ref. [29] explores the influence of $\chi^{(3)}$ effects in quadratic combs, which play a considerable role in microscale comb platforms. Experimental evidence of compact quadratic combs have only recently been observed in a 20-mm-long periodically poled lithium niobate waveguide[30] as well as MgO-doped lithium niobate bulk whispering gallery mode resonators[31,32]. Although prominent MI-like comb structures and a very low quadratic comb threshold were successfully observed in ref. [32], quadratic solitons have not yet been experimentally observed.

Here, we report successful generation of a quadratic microcomb soliton in an aluminium nitride (AlN) nanophotonic platform. We employ a degenerate OPO by pumping the device in the near-visible band around 780 nm to produce stable quadratic solitons in the near-infrared band near 1,560 nm. Our numerical simulations describe a unique OPO detuning model that suggests the presence of multiple temporal patterns with distinct comb structures before the single-soliton state sets in. Additionally, the OPO-driven Pockels soliton microcomb features a low comb threshold, a deterministic soliton generation pathway and high pump-to-soliton conversion efficiency compared to its equivalent Kerr counterpart. Our work suggests the great potential of Pockels soliton microcombs for future nonlinear photonic applications.

Results

The traditional route of producing frequency combs near the OPO frequency, particularly in the mid-infrared, uses a high-power, femtosecond pulsed pump[33,34]. In a cavity containing both $\chi^{(3)}$ and $\chi^{(2)}$ nonlinearities, four-wave mixing expands the frequency comb through a Kerr ($\chi^{(3)}$) process with a coupling strength of $g^{(3)}$, which is then spectrally translated to the OPO frequency through $\chi^{(2)}$ coupling with a coupling strength of $g^{(2)}$. OPO combs may also arise from a strong continuous wave (c.w.) tone pumping a doubly resonant cavity containing a $\chi^{(2)}$ medium. Cavity resonance near the OPO

---

[1]Department of Electrical Engineering, Yale University, New Haven, CT, USA. [2]Department of Optics and Optics Engineering, University of Science and Technology of China, Hefei, Anhui, China. ✉e-mail: hong.tang@yale.edu

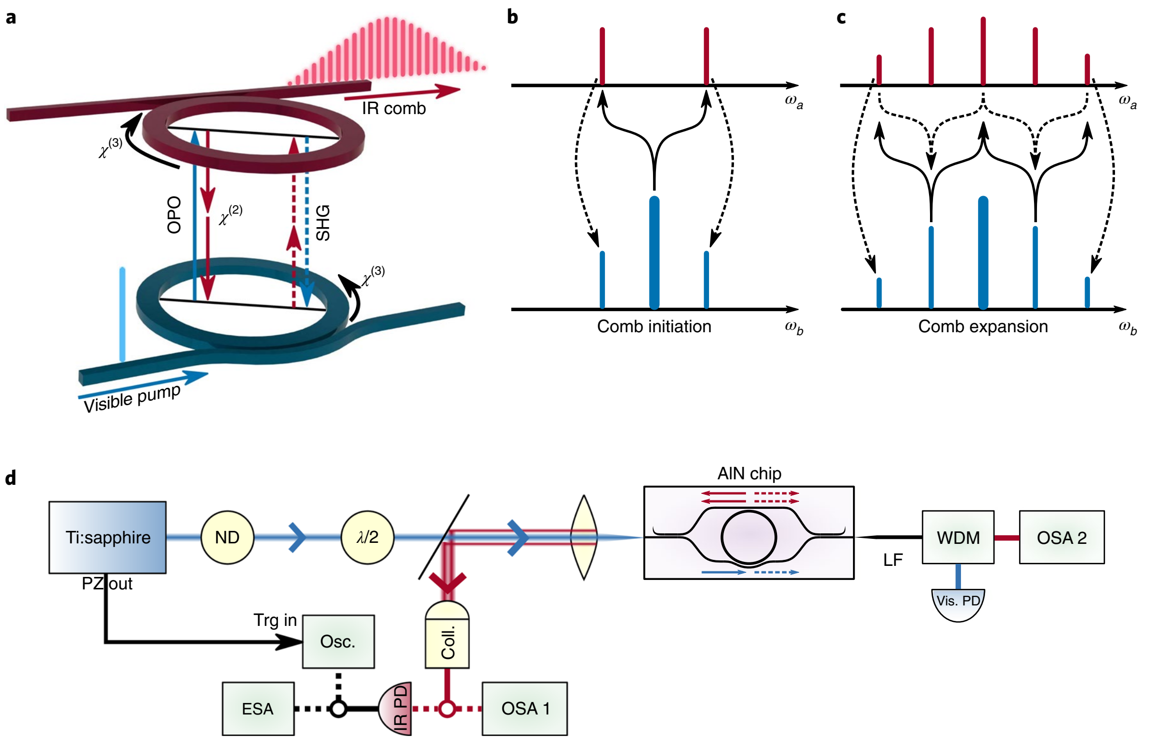

Fig. 1 | Schematic of the Pockels microcomb in AlN microresonators. a, Quadratic comb generation from a c.w. pump in our AlN microring system, possessing strong $\chi^{(2)}$ nonlinearity. The AlN microring is idealized as two independent cavities that are coherently coupled by the $\chi^{(2)}$ effect. **b**, In the initiation phase, a near-visible pump produces infrared frequencies, while simultaneous SHG phase-matching produces near-visible frequencies. **c**, Back-to-back OPO, SHG and SFG expand the frequency comb at both the pump (ω_b, blue) and OPO (ω_a, red) frequencies. The solid and dashed arrows refer to OPO and SHG/SFG, respectively. **d**, Simplified measurement schematic. Transparent lines refer to free-space beams. Dashed lines refer to optional measurements following the infrared collimator. Scattered infrared light is monitored on optical spectrum analyser (OSA) 2 throughout the measurement. NS, neutral-density filter; PZ, piezo tuning voltage; Trg in; trigger for the time-domain measurement; WDM, wavelength-division multiplexer; Coll., collimator; Osc., oscillator; ESA, electrical spectrum analyser; IR PD, infrared photodetector; Vis PD, visible photodetector; LF, lensed fibre. Full descriptions of the components are provided in the Methods.

frequency excites sufficient nonlinear gain to produce emissions in the OPO band. If the $\chi^{(2)}$ phase-matching bandwidth is sufficiently broad, both degenerate ($\omega_a=\omega_b/2$) and non-degenerate ($\omega_a\neq\omega_b/2$) OPO phase-matching may be satisfied simultaneously, resulting in a narrowband comb near the OPO frequency. Additional sidebands may arise near the pump due to SFG of the OPO comb lines. This type of comb has already been realized in a bulk cavity Pockels comb operating in the OPO mode under a c.w. pump in both degenerate and non-degenerate phase-matching conditions[24].

Our on-chip implementation of an AlN microring system is idealized in Fig. 1a, modelled as two independent cavities coupled by the $\chi^{(2)}$ effect, akin to a triply resonant OPO[14,35,36]. This resonant cavity system contains an infrared mode with frequency ω_a (red) as well as a visible mode with frequency ω_b (blue). A Pockels microcomb is realized when the $\chi^{(2)}$ nonlinearity is sufficiently strong to promote back-to-back energy exchange between the two mode families, that is, simultaneous OPO and SHG. As the power of the infrared signal and idler increases, sidebands arise in the near-visible band via SHG of the signal and idler, as shown in Fig. 1b. The Pockels comb is initiated when the SHG lines reach their respective OPO threshold and seed the cascaded three-wave mixing process. This cascaded $\chi^{(2)}$ process occurs with a coupling strength of $[g^{(2)}]^2/\kappa_b$ where κ_b is the amplitude decay rate at near-visible mode b (ref. [37]). The infrared and near-visible combs expand via cascaded OPO and SHG/SFG, respectively, shown in Fig. 1c, again with a coupling strength of $[g^{(2)}]^2/\kappa_b$. A background-free bright soliton may then arise when the OPO modes have anomalous dispersion[29].

Comb characterization. Our experimental set-up, shown in Fig. 1d and described in detail in the Methods, consists of a dually coupled AlN microring resonator that is phase-matched between 1,560-nm and 780-nm modes. This device is pumped by a tunable, narrow-linewidth (~50 kHz) Ti:sapphire laser centred around 780 nm. The AlN microring is identical to that presented in ref. [36] which achieves frequency conversion via modal phase-matching between infrared TM_{00} and near-visible TM_{20} modes (TM, transverse magnetic) in a microring (width, 1.2 µm; height, 1.0 µm; radius, 60 µm). The near-visible pump mode is near-critically coupled with a loaded optical quality (Q) factor of 2.0×10^5 and the infrared signal/idler mode is slightly under-coupled with a loaded optical Q factor of 6.0×10^5. This device exhibits a 12-mW OPO threshold and 17% pump-to-OPO conversion efficiency limited by the optical Q factors and coupling efficiencies at each mode. This device is capable of both degenerate and non-degenerate OPO, while a total phase-matching bandwidth of 180 nm across the C-band is observed in the case of non-degenerate OPO.

To investigate quadratic comb behaviour, we set the temperature of an external heater beneath the chip for the degenerate phase-matching condition at low power and then boosted the on-chip pump power to ~80 mW (five times the OPO threshold). We recorded a total signal and idler power of ~14 mW at this pump power, which agrees with established OPO power relations[36,38]. Notably, the on-chip visible pump power and infrared OPO power are less than the estimated Kerr comb thresholds of ~370 mW and ~40 mW for visible and infrared wavelengths, respectively[39].

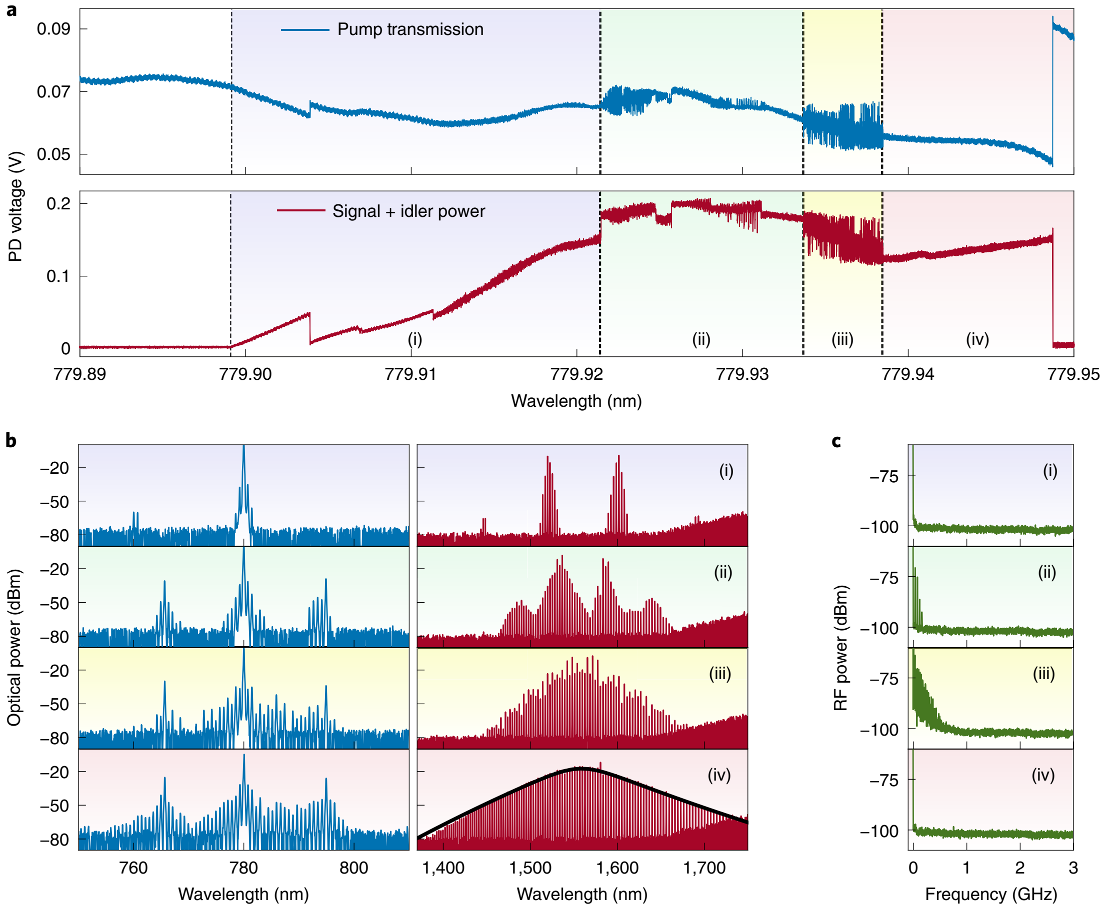

Fig. 2 | Comb detuning and power spectra. a, Near-visible transmission (blue) and infrared power (red) recorded as the microring resonance is scanned from blue-detuned to red-detuned states. Four distinct comb states are observed and labelled (i) to (iv). **b**,**c**, Optical (**b**) and radio-frequency (RF) (**c**) spectra of the comb states observed in **a**. A sech^2 fit is applied to the infrared optical spectrum in (iv). The RF spectra in (i) and (iv) are equivalent to the measurement noise floor. All measurements are performed at an on-chip pump power of 80 mW.

The interplay between $\chi^{(2)}$ and $\chi^{(3)}$ effects is described in more detail in our modelling below, as well as in Supplementary Note 3.

Figure 2a shows the OPO power trace as the pump is scanned over the resonance at a moderate speed of ~25 GHz s^{-1}. We observe Kerr comb-like distinct discontinuities and assign them into four different operation regimes, labelled (i) to (iv), corresponding to the distinct comb states in Fig. 2b. We note that all four comb states exhibit relatively slow dynamics and can be accessed by manually tuning the laser frequency.

State (i) lies just above the OPO threshold. Its optical spectrum in Fig. 2b(i) reveals two non-degenerate comb-like structures due to an OPO process as presented in ref. [24]. The near-visible spectrum shows multiple sidebands near the 780-nm pump due to SFG of the OPO combs. Little SHG of the OPO combs is observed, suggesting these lines lie beyond the SHG phase-matching bandwidth. We do not attribute the non-degenerate combs to four-wave mixing, as the infrared power (~14 mW) is below the estimated Kerr comb threshold (~40 mW). Furthermore, a numerical simulation excluding $\chi^{(3)}$ effects predicts similar non-degenerate comb behaviour, although the presence of $\chi^{(3)}$ effects may expand the combs through non-degenerate four-wave mixing (Supplementary Note 3). The jumps in the OPO power trace correspond to the progression of non-degenerate OPO combs towards degeneracy near 1,560 nm. The non-degenerate OPO combs exhibit low RF noise near the noise floor of our measurement set-up, as shown in Fig. 2c(i). This is expected, because the FSRs of signal and idler combs are larger than the detector bandwidth and there is no spectral overlap between these clustered combs. The near-visible RF spectra were not measured due to the strong pump tone near 780 nm overwhelming the RF signal.

The microcomb then transitions to state (ii), shown in Fig. 2b(ii),c(ii). This comb is identified by the appearance of two strong non-degenerate OPO tones near 1,520 nm and 1,590 nm that merge near degeneracy at 1,560 nm, as well as the emergence of strong SHG of these lines near 765 nm and 795 nm. The RF spectrum of this comb exhibits a low overall noise floor with strong beat notes at 42 MHz and its harmonics. This beating suggests the comb spectrum in Fig. 2b(ii) consists of a superposition of two non-degenerate OPO combs centred at 1,520 nm and 1,590 nm with a slight frequency offset on the order of tens of MHz near 1,560 nm. This offset is within the infrared resonance linewidth of ~200 MHz, which still fulfils the OPO phase-matching condition with a non-zero detuning from the cavity resonance frequency. Beating of additional comb lines is not observed within the detector bandwidth.

The non-degeneracy is pushed towards the degenerate OPO condition by further increasing the pump wavelength. The OPO comb power then enters a noisy, unstable state (iii) akin to modulation instability noise characteristic of a Kerr comb[11]. The OSA and RF spectra in Fig. 2b(iii),c(iii) show a comb spectrum resembling a Kerr MI comb with the maximum power centred at 1,560 nm and pronounced RF noise in the low frequency regime. In the $\chi^{(2)}$-driven case, such MI-like noise is attributed to FSR locking between the

1*f* and 2*f* frequency components[24,32]. Inspection of both near-visible and infrared spectra shows that both infrared and near-visible microcombs lock to an FSR of 361 GHz, limited by the resolution of the OSA. On further pump tuning, a low-noise soliton state (iv) is achieved after the noisy MI state. The optical power spectrum in Fig. 2b(iv) reveals a characteristic sech^2 spectral envelope, while SHG/SFG phase-matching is achieved over the entire near-visible comb bandwidth in the soliton state. The appearance of persistent strong peaks near 765 nm and 795 nm is an unexpected result in this experiment. We currently attribute these strong lines to wavelength-dependent parameters such as avoided mode crossings and/or wavelength-dependent coupling; this will be the subject of follow-up investigations. The RF power spectrum in Fig. 2c (iv) reveals RF noise near the measurement noise floor. Unlike a conventional Kerr soliton, the Pockels soliton optical spectrum is c.w.-background-free due to large spectral separation from the pump frequency. Applying a sech^2 fit to the soliton spectra reveals a 6.8-THz 3-dB optical bandwidth, corresponding to a 46-fs soliton pulse width. The spectral bandwidth of the soliton state is ultimately limited by the cavity dispersion at the OPO frequency ($D_2/2\pi \approx 15$ MHz), as predicted by previous theoretical studies[28,29].

The spectra in Fig. 2b demonstrate the progression of OPO phase-matching from non-degenerate (states (i)–(ii)) to degenerate OPO states (states (iii)–(iv)). Typically, degenerate and non-degenerate OPO comb states are accessed by varying the phase-matching temperature of the device[24]. We investigate the impact of the initial phase-matching condition by varying the chip temperature at a constant pump power in Supplementary Note 2. When tuned away from the degenerate phase-matching temperature, only non-degenerate comb states are supported and solitons such as that in Fig. 2b(iv) are not observed. Although these non-degenerate states show low noise akin to states (i) and (ii), our current results suggest that quadratic solitons are only achieved when the degenerate OPO phase-matching is satisfied. Our numerical simulation in Supplementary Note 3 suggests that single soliton states are possible in the case of large phase mismatching at relatively high pump powers; however, these pump powers are difficult to achieve in the current experiment and lead to significant instabilities in the comb spectrum.

Numerical simulation. Figure 2 depicts multiple comb states with distinct optical and RF spectra; however, few insights into the Pockels comb process can be gleaned from these data alone. We now turn to a numerical simulation to determine the origin of comb states (i) to (iv) and understand the dynamics of the comb detuning process shown in Fig. 2a. Although the dynamics of the Kerr microcomb system can be modelled by the Lugiato–Lefever equation with significant accuracy[40], such an analytical solution does not yet exist for the Pockels comb system. Numerical simulations in ref. [29] recently studied the interplay between $\chi^{(2)}$ and $\chi^{(3)}$ in an OPO-driven Pockels comb similar to that presented here. A sech-pulse solution was proposed in that work, but the solution derived therein assumes normal dispersion near the OPO frequency instead of the anomalous dispersion presented here. We use a modal expansion method of coupled mode equations including both $\chi^{(2)}$ and $\chi^{(3)}$ effects to gain insights on the spectra observed in Fig. 2. Details on the numerical simulation are provided in the Methods as well as in ref. [14].

The experiment in Fig. 2 suggests that scanning the pump laser frequency changes the OPO phase-matching condition and pushes the Pockels microcomb into the degenerate OPO state. Given the large thermal shift of the cavity resonance in Fig. 2a and that state (i) is always non-degenerate OPO, we assume the OPO process begins with an initial phase mismatch from the degenerate OPO condition of $\omega_b = 2\omega_a$, where $\omega_{b(a)}$ is the frequency of the visible (infrared) mode. We indicate the detuning of the pump from the degenerate phase-matching condition as the 'OPO detuning', described by $\omega_b - 2\omega_a = \xi\kappa_a$, where ξ is the initial phase mismatching parameter and κ_a is the total amplitude decay rate of the infrared mode *a*. We then sweep the pump frequency ω_p throughout the simulation to observe the impact due to this OPO detuning. An exemplary numerical simulation of our Pockels cavity system under a strong visible pump is shown in Fig. 3a for an initial phase mismatching of $\xi = 14$. As the pump is scanned across resonance, the onset of OPO is observed as a sharp increase in infrared photon number with a corresponding drop in the near-visible photon number. The time-domain waveform of state (i) reveals a Turing pattern corresponding to the superposition of *N* optical pulses in the microcavity. Figure 3b(i) shows the temporal envelope for a non-degenerate OPO comb with $N = 12$. The corresponding comb clusters in Fig. 3c (i) are separated by $N \times$ FSR from the degenerate OPO wavelength of 1,560 nm. Sharp changes in the infrared photon number are observed as the OPO detuning decreases further, similar to that observed in Fig. 2a. At each jump in photon number, the number of pulses decreases by 2 (that is, 14, 12, 10, ...) and spectral separation of each comb cluster from the degenerate OPO condition correspondingly decreases with decreasing *N*. Thus, the reduction in pulse number corresponds to increasing degeneracy of the Pockels microcomb, as shown in the upper panel in Fig. 3a. This process continues as the comb enters state (ii) as in Fig. 3c(ii). Even-numbered Turing patterns are still visible ($N = 8$), and the pulse number continues to decrease 2 by 2 with further OPO detuning. However, one pulse begins to grow in intensity as the comb lines close to the degeneracy point become stronger, as shown in Fig. 3b(ii). This strong pulse grows further in intensity as the comb enters the degenerate state (iii) and odd pulse numbers arise in the cavity starting at $N = 5$, as shown in Fig. 3b(iii),c(iii). Here, the intracavity photon number and temporal amplitude exhibit considerable instability compared to states (i) and (ii) and the pulse number begins to decrease 1 by 1 until $N = 1$ (that is, 5, 4, 3, 2, 1), realizing a single pulse in the time domain. The corresponding infrared comb exhibits a sech^2 power spectrum similar to that shown in Fig. 2b(iv). This rapid reorganization of the pulse number probably gives rise to the MI-like noise observed in the experiment. The OPO detuning process can be seen in its entirety in Supplementary Video 1. The near-visible temporal profiles in Fig. 3b and a discussion of their spectral profiles are provided in Supplementary Note 3.

The analysis outlined in the Methods suggests that the coupling rate of the cascaded $\chi^{(2)}$ process is approximately five times larger than the four-wave mixing process and should be dominant in our AlN microring. Thus, we attribute the above results to a cascaded $\chi^{(2)}$ process rather than OPO followed by conventional four-wave mixing. The interplay between $\chi^{(2)}$ and $\chi^{(3)}$ effects in the OPO-driven Pockels comb has been studied in detail in ref. [29] as well as in Supplementary Note 3 by removing all $\chi^{(3)}$ interactions and re-running the simulation. Low-noise Turing patterns are observed in 'pure' Pockels system; however, single soliton states are not stable in the absence of $\chi^{(3)}$ effects. Moreover, the absence of $\chi^{(3)}$ effects yields a narrower comb profile at both infrared and near-visible bands compared to the case with both $\chi^{(2)}$ and $\chi^{(3)}$ effects. These findings suggest that the Pockels comb process is primarily driven by $\chi^{(2)}$ effects, while weak $\chi^{(3)}$ interactions further expand and stabilize the spectral and temporal profiles, respectively.

Each of the waveforms in Fig. 3b is stable and should correspond to the temporal waveform of the corresponding comb state ((i) to (iv)) in Fig. 2b. Our simulations indicate that the beating of OPO signal/idler pairs in our system forms a regular periodic potential; the deterministic reduction in the pulse number in the 2 by 2 fashion described above smoothly induces soliton states without going through large MI noise. This smooth reduction in optical pulse number yields a nearly unity soliton generation fidelity with relatively slow dynamics, as observed in Fig. 2.

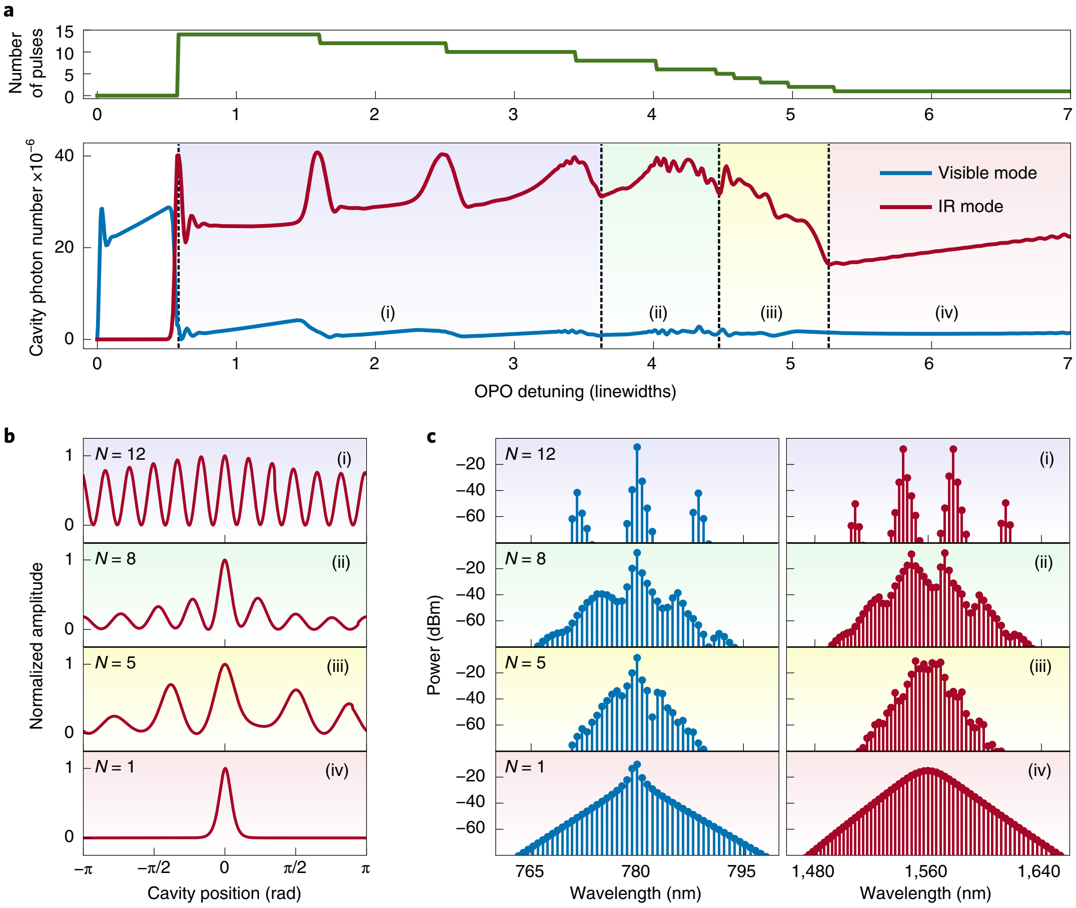

Fig. 3 | Numerical simulation of the Pockels microcomb. a, Evolution of the near-visible (blue) and infrared (red) cavity photon number as the pump is red-detuned. The number of optical pulses (*N*) is shown above as a reference. Comb states (i) to (iv) are labelled following the convention in Fig. 2. **b**,**c**, Simulated temporal (**b**) and spectral (**c**) components of each comb state in **a**. All simulations are performed at an on-chip pump power of 80 mW. The evolution of the whole process is available in Supplementary Video 1.

Soliton stability and efficiency. We further investigate the soliton stability and pump-to-comb power conversion ratio to provide an experimental comparison to our simulations above. Figure 4a presents an overlay of 34 successive comb power traces recorded at an on-chip power of 80 mW and a tuning speed of 25 GHz s^{-1} by scanning the laser cavity piezo. The four OPO comb states in Fig. 2a are observed for all 34 comb traces. A slightly reduced overlay density is observed in states (ii) and (iii) due to unstable RF and intensity noise as observed in Fig. 2. All of the traces then converge to the single soliton state. We note that the high soliton fidelity was achieved using a simple cavity piezo scan and solitons are passively stable for tens of minutes, after which laser drift and/or temperature fluctuations may revert the soliton to state (iii) or off-resonance.

The pump power dependence was then probed by varying the power coupled to the waveguide via a neutral-density filter. By controlling the phase-matching temperature, Pockels microcombs and solitons may be generated at a relatively low threshold of 25 mW on-chip near-visible power, albeit with reduced bandwidth compared to that in Fig. 2b. A comb threshold of 28 mW is predicted from a recent derivation of the Pockels comb threshold[41] and is in strong agreement with the experimentally observed value.

We note that the 25-mW quadratic comb threshold observed here is nearly half the estimated Kerr comb threshold at infrared wavelengths (~40 mW) and more than an order of magnitude lower than that at near-visible wavelengths (~370 mW) calculated using the optical Q factors and n_2 of AlN at each wavelength[39]. This low threshold is due to the relatively large magnitude of $\chi^{(2)}$ susceptibility compared to $\chi^{(3)}$; indeed, the cascaded $\chi^{(2)}$ process has shown to be dominant over the $\chi^{(3)}$ process at moderate optical Q factors near 10^5 (ref. [42]). Quadratic comb thresholds as low as 85 μW have recently been reported in whispering gallery mode resonators[41], which is already comparable to current state-of-the-art values in Kerr microcomb systems[43].

The absence of a large erbium-doped fibre amplifier background commonly seen in Kerr microcombs allows us to directly collect the Pockels comb power near the OPO frequency. As the pump power increases further, the MI comb power increases to 19 mW, following the characteristic OPO power curve[36,38] (orange line in Fig. 4b,c). The soliton power begins to saturate to 10 mW after the pump power exceeds 75 mW. We then numerically verify this behaviour by sweeping the visible pump strength. The infrared photon number continuously increases with power in the $N > 1$ comb states, whereas the photon number begins to saturate in the $N = 1$ soliton state when the pump power exceeds 60 mW. This power dependence is explicitly shown in Supplementary Note 3. The infrared photon number is then converted to total infrared power and largely agrees with the pump power dependence observed in the experiment, shown as open triangle symbols in Fig. 4b,c. Our experimental and numerical results suggest the soliton power is clamped by an external mechanism unrelated to the traditional OPO process. At this time we believe the saturation of the soliton power is largely

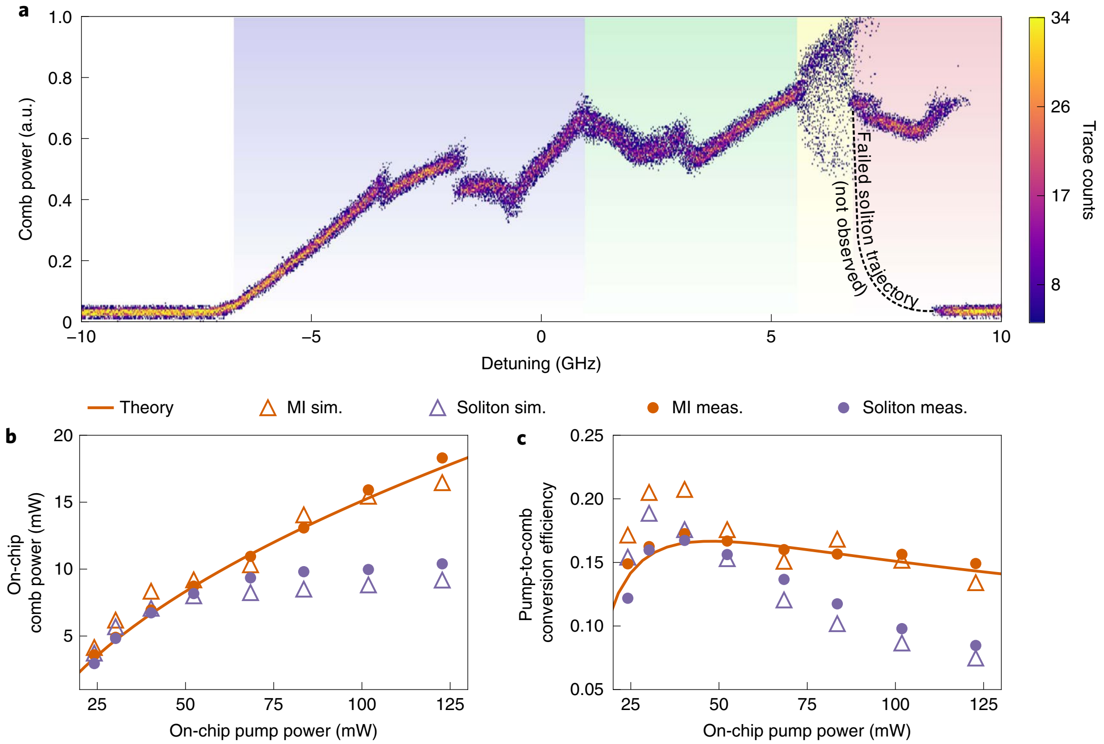

Fig. 4 | Robustness and power conversion efficiency of the Pockels comb. **a**, Histogram of 34 successive comb power traces. The colour bar corresponds to the probability of trace overlap. The trajectory of a failed soliton state is shown as a reference, which did not happen in our experiment. **b**,**c**, On-chip OPO comb power (**b**) and pump-to-comb conversion efficiency (**c**). The MI comb power (orange) increases with near-visible pump power, while the on-chip soliton power (purple) saturates to 10 mW. The power and efficiency calculated by the numerical simulation is shown as orange and purple triangles for the MI and soliton states, respectively.

due to the dispersion of the sech^2 envelope of our system, similar to that observed in the Kerr soliton case[44].

Normalizing the on-chip infrared comb power to the on-chip near-visible power yields the on-chip efficiency shown in Fig. 4c. We observe a maximum efficiency of 17% for both the MI state and soliton state, which then saturates to 15% in the MI state. The pump-to-soliton conversion efficiency rapidly depletes after the maximum value of 17% due to the saturated soliton power. The simulated efficiency (open triangles) is larger than the measured efficiency (filled circles) in the low-power regime, probably due to errors in simulating the comb near the Pockels comb threshold. This error is mitigated in the high power regime, where residual error is attributed to estimating d_2 and D_2 in our numerical simulation. The OPO power and efficiency in states (i) to (iii) scale nearly exactly with that predicted by OPO theory[36,38]. Intuitively, this can be thought of as spreading the available OPO power across many frequency components instead of the typical signal and idler pair. This can be confirmed by comparing the OPO power in Fig. 2a and the photon number in Fig. 3a across states (i) to (iv).

Discussion

The broad interest in microcomb solitons merits a discussion on the key differences between the Pockels- and Kerr-driven combs. In summary, our results suggest the quadratic soliton provides a compelling platform for low-threshold, high-fidelity and high-efficiency soliton generation. Our current results demonstrate a 17% maximum conversion efficiency for Pockels solitons, whereas Kerr bright solitons often have <5% pump-to-soliton conversion efficiency under typical coupling conditions. At high pump power regimes, our Pockels soliton maintains an 8.5% pump-to-soliton conversion efficiency whereas its equivalent Kerr soliton would exhibit an efficiency of 3.3% calculated at a similar pump power above threshold[44].

The Pockels soliton also exhibits relatively slow dynamics, which can be probed by hand tuning of the pump wavelength. Our numerical simulations suggest multiple Turing pattern states throughout the OPO detuning process. The smooth reduction in optical pulses into the single soliton state results in a nearly deterministic soliton generation pathway. This process is dominated by $\chi^{(2)}$ phase-matching, which can be well controlled compared to the fast dynamics experienced in the case of a Kerr soliton[11,45–47].

Of course, the benefits of the Pockels soliton come at the cost of large trade-offs, such as achieving optimal phase-matching, pumping at short wavelengths and a relatively immature theoretical understanding compared to Kerr combs. The main advantage of the Kerr soliton is its large optical bandwidth. $\chi^{(3)}$ phase-matching may be readily optimized over a wide range of frequencies, realizing octave-spanning solitons in a chip-integrated platform[48,49]. Our current quadratic soliton has a relatively limited 3-dB optical bandwidth of 6.8 THz. Similar to the Kerr case, the Pockels microcomb bandwidth may be limited by second-order dispersion at the OPO frequency[28,29]. Future work will investigate the importance of second-order dispersion on $\chi^{(2)}$ phase-matching to push future devices towards an octave in optical bandwidth.

Adoption of $\chi^{(2)}$ phase-matched geometries with optimal dispersion could realize broadband quadratic solitons. Although simultaneous quadratic and cubic phase-matching is difficult to realize by engineering the modal phase-matching and group-velocity dispersion, it could be achieved in quasi-phase-matched periodically poled lithium niobate[50,51] microring resonators for sustaining the quadratic comb over a broad frequency range. Octave-spanning quadratic combs would naturally open routes to facile $f-2f$ self-referencing[17].

The dual-band nature of quadratic solitons and high conversion efficiency would allow for direct detection of the comb carrier envelope offset frequency (f_{ceo}) if octave-spanning comb spectra could be achieved. Such quadratic combs would simplify comb stabilization for optical clocks[4,5] and exoplanet observation[6].

Online content

Any methods, additional references, Nature Research reporting summaries, source data, extended data, supplementary information, acknowledgements, peer review information; details of author contributions and competing interests; and statements of data and code availability are available at https://doi.org/10.1038/s41566-020-00704-8.

Received: 15 May 2020; Accepted: 15 September 2020;
Published online: 19 October 2020

References

1. Kippenberg, T. J., Holzwarth, R. & Diddams, S. A. Microresonator-based optical frequency combs. *Science* **332**, 555–559 (2011).
2. Gaeta, A. L., Lipson, M. & Kippenberg, T. J. Photonic-chip-based frequency combs. *Nat. Photon.* **13**, 158–169 (2019).
3. Spencer, D. T. et al. An optical-frequency synthesizer using integrated photonics. *Nature* **557**, 81–85 (2018).
4. Papp, S. B. et al. Microresonator frequency comb optical clock. *Optica* **1**, 10–14 (2014).
5. Newman, Z. L. et al. Architecture for the photonic integration of an optical atomic clock. *Optica* **6**, 680–685 (2019).
6. Suh, M.-G. et al. Searching for exoplanets using a microresonator astrocomb. *Nat. Photon.* **13**, 25–30 (2019).
7. Obrzud, E. et al. A microphotonic astrocomb. *Nat. Photon.* **13**, 31–35 (2019).
8. Picqué, N. & Hänsch, T. W. Frequency comb spectroscopy. *Nat. Photon.* **13**, 146–157 (2019).
9. Dutt, A. et al. On-chip dual-comb source for spectroscopy. *Sci. Adv.* **4**, e1701858 (2018).
10. Kues, M. et al. Quantum optical microcombs. *Nat. Photon.* **13**, 170–179 (2019).
11. Herr, T. et al. Universal formation dynamics and noise of Kerr-frequency combs in microresonators. *Nat. Photon.* **6**, 480–487 (2012).
12. Kippenberg, T. J., Gaeta, A. L., Lipson, M. & Gorodetsky, M. L. Dissipative Kerr solitons in optical microresonators. *Science* **361**, eaan8083 (2018).
13. Stern, B., Ji, X., Okawachi, Y., Gaeta, A. L. & Lipson, M. Battery-operated integrated frequency comb generator. *Nature* **562**, 401–405 (2018).
14. Guo, X. et al. Efficient generation of a near-visible frequency comb via Cherenkov-like radiation from a Kerr microcomb. *Phys. Rev. Appl.* **10**, 014012 (2018).
15. He, Y. et al. Self-starting bi-chromatic $\mathrm{LiNbO_3}$ soliton microcomb. *Optica* **6**, 1138–1144 (2019).
16. Liu, X. et al. Beyond 100-THz-spanning ultraviolet frequency combs in a non-centrosymmetric crystalline waveguide. *Nat. Commun.* **10**, 2971 (2019).
17. Hickstein, D. D. et al. Ultrabroadband supercontinuum generation and frequency-comb stabilization using on-chip waveguides with both cubic and quadratic nonlinearities. *Phys. Rev. Appl.* **8**, 014025 (2017).
18. Xue, X. et al. Second-harmonic-assisted four-wave mixing in chip-based microresonator frequency comb generation. *Light Sci. Appl.* **6**, e16253 (2017).
19. Yang, Q.-F., Yi, X., Yang, K. Y. & Vahala, K. Stokes solitons in optical microcavities. *Nat. Phys.* **13**, 53–57 (2017).
20. Skryabin, D. V. & Champneys, A. R. Walking cavity solitons. *Phys. Rev. E* **63**, 066610 (2001).
21. Ulvila, V., Phillips, C. R., Halonen, L. & Vainio, M. Frequency comb generation by a continuous-wave-pumped optical parametric oscillator based on cascading quadratic nonlinearities. *Opt. Lett.* **38**, 4281–4284 (2013).
22. Ricciardi, I. et al. Frequency comb generation in quadratic nonlinear media. *Phys. Rev. A* **91**, 063839 (2015).
23. Mosca, S. et al. Direct generation of optical frequency combs in χ^2 nonlinear cavities. *Nanophotonics* **5**, 316–331 (2016).
24. Mosca, S. et al. Modulation instability induced frequency comb generation in a continuously pumped optical parametric oscillator. *Phys. Rev. Lett.* **121**, 093903 (2018).
25. Jankowski, M. et al. Temporal simultons in optical parametric oscillators. *Phys. Rev. Lett.* **120**, 053904 (2018).
26. Leo, F. et al. Frequency-comb formation in doubly resonant second-harmonic generation. *Phys. Rev. A* **93**, 043831 (2016).
27. Hansson, T. et al. Quadratic soliton combs in doubly resonant second-harmonic generation. *Opt. Lett.* **43**, 6033–6036 (2018).
28. Villois, A. & Skryabin, D. V. Soliton and quasi-soliton frequency combs due to second harmonic generation in microresonators. *Opt. Express* **27**, 7098–7107 (2019).
29. Villois, A., Kondratiev, N., Breunig, I., Puzyrev, D. N. & Skryabin, D. V. Frequency combs in a microring optical parametric oscillator. *Opt. Lett.* **44**, 4443–4446 (2019).
30. Ikuta, R., Asano, M., Tani, R., Yamamoto, T. & Imoto, N. Frequency comb generation in a quadratic nonlinear waveguide resonator. *Opt. Express* **26**, 15551–15558 (2018).
31. Hendry, I. et al. Experimental observation of internally pumped parametric oscillation and quadratic comb generation in a χ^2 whispering-gallery-mode microresonator. *Opt. Lett.* **45**, 1204–1207 (2020).
32. Szabados, J. et al. Frequency comb generation via cascaded second-order nonlinearities in microresonators. *Phys. Rev. Lett.* **124**, 203902 (2020).
33. Schliesser, A., Picqué, N. & Hänsch, T. W. Mid-infrared frequency combs. *Nat. Photon.* **6**, 440–449 (2012).
34. Herr, S. J. et al. Frequency comb up- and down-conversion in synchronously driven χ^2 optical microresonators. *Opt. Lett.* **43**, 5745–5748 (2018).
35. Guo, X., Zou, C.-L., Jung, H. & Tang, H. X. On-chip strong coupling and efficient frequency conversion between telecom and visible optical modes. *Phys. Rev. Lett.* **117**, 123902 (2016).
36. Bruch, A. W., Liu, X., Surya, J. B., Zou, C.-L. & Tang, H. X. On-chip χ^2 microring optical parametric oscillator. *Optica* **6**, 1361–1366 (2019).
37. Li, M., Zou, C.-L., Dong, C.-H., Ren, X.-F. & Dai, D.-X. Enhancement of second-harmonic generation based on the cascaded second-and third-order nonlinear processes in a multimode optical microcavity. *Phys. Rev. A* **98**, 013854 (2018).
38. Breunig, I. Three-wave mixing in whispering gallery resonators. *Laser Photon. Rev.* **10**, 569–587 (2016).
39. Liu, X. et al. Integrated high-*Q* crystalline AlN microresonators for broadband Kerr and Raman frequency combs. *ACS Photonics* **5**, 1943–1950 (2018).
40. Herr, T. et al. Temporal solitons in optical microresonators. *Nat. Photon.* **8**, 145–152 (2014).
41. Szabados, J., Sturman, B. & Breunig, I. Frequency comb generation threshold in $\chi^{(2)}$ optical microresonators. Preprint at https://arxiv.org/abs/2007.05287 (2020).
42. Boyd, R. W. *Nonlinear Optics* (Elsevier, 2003).
43. Zhang, S. et al. Sub-milliwatt-level microresonator solitons with extended access range using an auxiliary laser. *Optica* **6**, 206–212 (2019).
44. Bao, C. et al. Nonlinear conversion efficiency in Kerr frequency comb generation. *Opt. Lett.* **39**, 6126–6129 (2014).
45. Gong, Z. et al. High-fidelity cavity soliton generation in crystalline AlN micro-ring resonators. *Opt. Lett.* **43**, 4366–4369 (2018).
46. Brasch, V., Geiselmann, M., Pfeiffer, M. H. & Kippenberg, T. J. Bringing short-lived dissipative Kerr soliton states in microresonators into a steady state. *Opt. Express* **24**, 29312–29320 (2016).
47. Brasch, V. et al. Photonic chip-based optical frequency comb using soliton Cherenkov radiation. *Science* **351**, 357–360 (2016).
48. Pfeiffer, M. H. et al. Octave-spanning dissipative Kerr soliton frequency combs in $\mathrm{Si_3N_4}$ microresonators. *Optica* **4**, 684–691 (2017).
49. Li, Q. et al. Stably accessing octave-spanning microresonator frequency combs in the soliton regime. *Optica* **4**, 193–203 (2017).
50. Lu, J. et al. Periodically poled thin-film lithium niobate microring resonators with a second-harmonic generation efficiency of 250,000%/W. *Optica* **6**, 1455–1460 (2019).
51. Chen, J.-Y. et al. Ultra-efficient frequency conversion in quasi-phase-matched lithium niobate microrings. *Optica* **6**, 1244–1245 (2019).

Methods

Measurement scheme. We probed the whole process using the experimental set-up shown in Fig. 1d. The pump source is a free-space c.w. Ti:sapphire laser (700–1,000 nm, M2 SolsTiS), while the incident power and polarization are controlled via a neutral-density filter (ND) and half-wave plate ($\lambda/2$), respectively. The infrared comb is mainly emitted towards the pump facet, which is then reflected off a dichroic mirror and collected in a variable-zoom collimator (Thorlabs CFC-11X-C) for efficient fibre collection. The infrared comb is probed via a high-sensitivity optical spectrum analyser (OSA 1, Yokogowa 6374) or collected in a high-speed photodetector. The photodetector signal can then be viewed on an electrical spectrum analyser (ESA, Advantest U3751) or in the time domain with an oscilloscope (Tektronix MDO3014). The Ti:sapphire piezo tuning voltage (PZ out) is used as a trigger for the time-domain measurement (Trg in). Approximately 1–5% of infrared light is scattered towards the transmission port of the chip, which is collected via a lensed fibre and separated from the near-visible transmission via a fibre-based wavelength division multiplexer (WDM). The scattered infrared light is monitored on a separate OSA (OSA 2, Hewlett Packard 70004A) to record the comb spectra throughout the measurement. The near-visible transmission is monitored on a high-speed near-visible photodetector.

Numerical simulations. The dynamics of the optical modes in the resonator are described by the Hamiltonian

$$\begin{aligned}\mathcal{H} = \; & \textstyle\sum_{j=-N_1}^{N_1} \hbar\Delta_j^a a_j^\dagger a_j + \sum_{j=-N_2}^{N_2} \hbar\Delta_j^b b_j^\dagger b_j \\ & + \mathcal{H}_{\chi^{(2)}} + \mathcal{H}_{\chi^{(3)}} + \hbar\epsilon_{\mathrm{p}}(b_0 + b_0^\dagger)\end{aligned} \tag{1}$$

where a_j and b_j represent the infrared and visible bosonic operators of the jth mode. Equation (1) encompasses many nonlinear processes[37], notably:

- The conventional $\chi^{(2)}$ process $(a+a\rightarrow b)$ and $(b\rightarrow a+a)$ with coupling strength $g^{(2)}$
- The conventional $\chi^{(3)}$ process $(a_j+a_j\rightarrow a_{j+1}+a_{j-1})$ with coupling strength $g_{aa}^{(3)}$ (equivalently, the $\chi^{(3)}$ process at mode b is represented by $g_{bb}^{(3)}$ and the cross-Kerr process between modes a and b is represented by $g_{ab}^{(3)}$)
- The cascaded $\chi^{(2)}$ process $(a_j+a_j\rightarrow b\rightarrow a_{j+1}+a_{j-1})$ and its inverse with coupling strength $[g^{(2)}]^2/(-i\delta_b-\kappa_b)$, where δ_b is the detuning between the generated photons at mode b and the cavity resonance
- We note that all three of these processes cascade together in the microresonator and do not exist independently. This cascading effect can also be observed in ref. [29]. Our previous theoretical study of SHG in the presence of both $\chi^{(2)}$ and $\chi^{(3)}$ nonlinear processes revealed that the cascaded $\chi^{(2)}$ process (Pockels comb) may only combine with the traditional $\chi^{(3)}$ process (Kerr comb) when their coupling strengths have similar magnitudes[37]. This interference occurs when $[g^{(2)}]^2/\kappa_b \approx g^{(3)}$, where $[g^{(2)}]^2/\kappa_b$ is the effective coupling rate of the cascaded $\chi^{(2)}$ process and $g^{(3)}$ is the coupling rate of the four-wave mixing process. We find that $[g^{(2)}]^2/\kappa_b$ is five times larger than $g^{(3)}$ using the relevant parameters given in the following, indicating that the cascaded $\chi^{(2)}$ mechanism is largely dominant over the conventional four-wave mixing process.

An external near-visible pump with power P_{in} and detuning from the cold-cavity resonance δ is introduced near mode b_0 with strength $\epsilon_{\mathrm{p}} = \sqrt{\frac{2\kappa_{b0,\mathrm{ex}}P_{\mathrm{in}}}{\hbar\omega_{\mathrm{p}}+\delta}}$. The mode frequencies of each family are given by $\omega_j=\omega_0+d_1j+d_2j^2/2$ and $\Omega_j=\Omega_0+D_1jD_2j^2/2$ for modes a and b, respectively. d_N and D_N refer to their Nth order dispersion coefficients. The detunings of each mode family relative to a pump field near b_0 with magnitude δ are given by $\Delta_j^a = d_2j^2-\delta$ and $\Delta_j^b = \Omega(D_1-d_1)j + D_2j^2 - 2(\omega_0+\delta)$. $\mathcal{H}_{\chi^{(2)}}$ denotes the $\chi^{(2)}$ effect in the microresonator with strength

$$\mathcal{H}_{\chi^{(2)}} = \textstyle\sum_{j,k,l} \hbar g_j^{(2)}(a_j a_k b_l^\dagger + a_j^\dagger a_k^\dagger b_l) \tag{2}$$

The sum $j+k=l$ denotes the phase-matching condition between modes a_j, a_k and b_l. $\mathcal{H}_{\chi^{(3)}}$ represents the Kerr (within one mode family) and cross-Kerr (between mode families) effects. We consider the phase mismatching due to the large thermal shift at high pump power via $\omega_b-2\omega_a=\xi\kappa_a$, where ξ is the initial phase mismatching from the degenerate OPO condition $\omega_b=2\omega_a$.

Under conditions of a strong external pump near mode b_0, the cavity field near the pump mode can be approximated as a classical field. The dynamics of the system are solved through the Heisenberg equation

$$\begin{aligned}\frac{\mathrm{d}}{\mathrm{d}t}a_j = \; & (-i\Delta_j^a - \kappa_j^a)a_j - i\textstyle\sum_{k,l} 2g_{jkl}^{(2)}\delta(j+k-l)a_k^\dagger b_l \\ & -i\textstyle\sum_{kln} 2g_{jkln}^{(3)aa} a_k^\dagger a_l a_n - i\sum_{kln} g_{jkln}^{(3)ab} a_k b_n^\dagger b_l\end{aligned} \tag{3}$$

$$\begin{aligned}\frac{\mathrm{d}}{\mathrm{d}t}b_j = \; & (-i\Delta_j^b - \kappa_j^b)b_j - i\textstyle\sum_{k,l} 2g_{klj}^{(2)} a_k a_l - i\sum_{kln} 2g_{jkln}^{(3)bb} b_k^\dagger b_l b_n \\ & -i\textstyle\sum_{kln} g_{nkjl}^{(3)ab} a_n^\dagger a_k b_l - i\epsilon_{\mathrm{p}}\delta_D(j-p)\end{aligned} \tag{4}$$

where $\delta_D(j-p)$ is the detuning of the pump from mode j. The Heisenberg equations are solved by the fast Fourier transform method to increase computational efficiency[14] and are evolved in time by a fourth-order Runge–Kutta method. Time steps and detunings are normalized to κ_a. We take the dispersion values as $d_1/2\pi=363$ GHz, $D_1/2\pi=351$ GHz, $d_2/2\pi=20$ MHz and $D_2/2\pi=34$ MHz and neglect high-order dispersion. The nonlinear coupling strengths are estimated from the mode overlaps and material $\chi^{(2)}$ and $\chi^{(3)}$ values as $g^{(2)}/2\pi=0.1$ MHz, $g_{aa}^{(3)}/2\pi=1.5$ Hz, $g_{bb}^{(3)}/2\pi=15$ Hz and $g_{ab}^{(3)}/2\pi=17$ Hz. The nonlinear coupling rates and loss rates are assumed to be wavelength-independent due the limited comb bandwidth.

Data availability

The data that support the plots within this paper and other findings of this study are available from the corresponding author upon reasonable request.

Acknowledgements

This work is supported by DARPA SCOUT (W31P4Q-15-1-0006). H.X.T. acknowledges support from DARPA's ACES programmes as part of the Draper-NIST collaboration (HR0011-16-C-0118) and a NSF EFRI grant (EFMA-1640959), as well as from the David and Lucile Packard Foundation. We thank Y. Sun, S. Reinhart, K. Woods and M. Rooks for assistance with device fabrication.

Author contributions

A.W.B. and H.X.T. conceived the experimental design. A.W.B. performed device fabrication, measurements and data analysis, with assistance from X.L., Z.G. and J.B.S. M.L. and C.-L.Z. performed numerical simulations and provided theoretical support. A.W.B. and H.X.T. wrote the manuscript, with input from all other authors. H.X.T. supervised the project.

Competing interests

The authors declare no competing interests.

Additional information

Supplementary information is available for this paper at https://doi.org/10.1038/s41566-020-00704-8.

Correspondence and requests for materials should be addressed to H.X.T.

Reprints and permissions information is available at www.nature.com/reprints.